Chapter 2: Mechanics Background

The fundamental mechanics principals used throughout the current work will be reviewed in this chapter beginning with contact (indentation) mechanics and a comparison of indentation techniques with traditional mechanical testing. This is followed by an introduction to analytical viscoelasticity, the mathematical framework commonly used in the study of time-dependent mechanical behavior. Third is a discussion of the properties and mechanics of composite materials, and how these properties relate to those of the component phases. Fourth, a brief explication of computer-aided finite element analysis is presented. Finally, a short section illustrates the ways in which these mechanical principles will be applied in the current work.

2.1 Contact Mechanics and Indentation Testing

Experimental contact mechanics testing has become extremely popular in the last decade, due to both the commercialization of dedicated indentation testing instruments and to advances in the practical and experimental understanding of performing contact mechanics experiments. After a brief introduction to modern nanoindentation, the fundamental elasticity solutions for mechanical testing using spherical and conical/pyramidal indenters will be discussed, along with elastic-plastic ("Oliver-Pharr") analysis and a discussion of the commercial indentation testing devices employed in the current work.

2.1.1 Indentation Testing Advantages

Traditional mechanical testing, such as a tensile test, involves the gripping of a sample with an approximately constant cross-sectional area (A_0) and pulling (or pushing in compression) in a direction perpendicular to the cross-section. A large volume V of material is loaded during this type of test, equal to the product of the sample gage length (l) and A and V is similar in magnitude to the total sample volume V_0 (less only the gripped region). In contrast, in contact mechanical testing a probe with known or calibrated shape is brought down onto a flat surface of material. The total sample volume V_0 can be substantially larger than the volume of material mechanically tested, V (Figure 2-1).

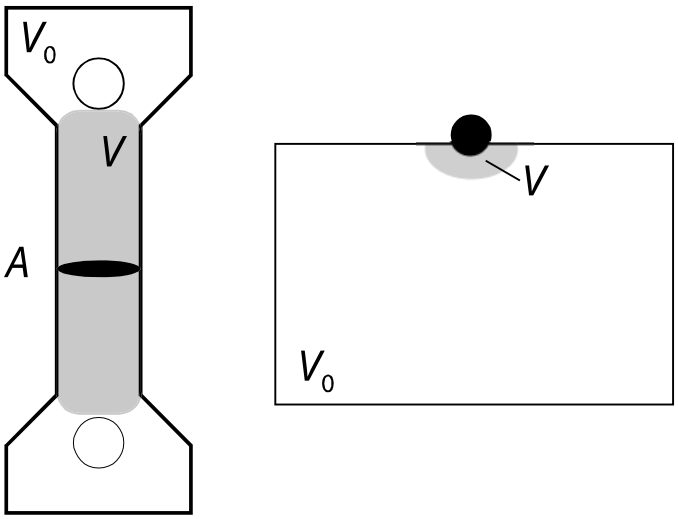

Figure 2-1: Mechanically tested volume of material V versus total sample volume V_0 for (left) tensile and (right) contact mechanical testing conditions.

Thus, while a tensile test averages the mechanical response over the whole sample, a contact test measures local behavior. Contact mechanical testing has become popular for examining local variations in mechanical behavior because of this small ratio of V/V_0. Indentation testing at very small length scales has been frequently referred to as "nanoindentation".

The most important variable in performing a contact mechanical test is the selection of a tip shape. Flat punch tips are convenient in that the cross-sectional area of the contacted region is constant, but there are stress singularities at the edges. Particularly in small-scale contact testing, it can also be near-impossible to align the tip's flat parallel to the sample surface. Therefore two tip shapes dominate small-scale contact testing: spherical and conical/pyramidal (Figure 2-2). Spherical tips are advantageous in that there is a delayed onset of plastic deformation, while conical/pyramidal tips are exactly the opposite since there is usually an immediate onset of plasticity and thus elastic-plastic deformation even at small displacements. In conical/pyramidal tips there is also the advantage of geometric similarity—there is no intrinsic length-scale associated with the size of the tip, and indentation tests at large loads result in deformation patterns that are scaled up from indentation tests at small loads. A disadvantage in the use of spherical and conical tips is that load is no longer a linear function of displacement, as is the case

for a homogeneous tensile test or a flat-punch indentation test, due to the changes in tip-sample contact area as the tip is pressed further into the surface.

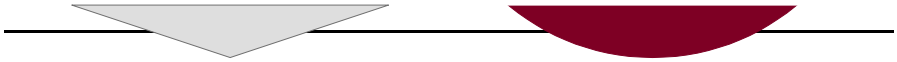

Figure 2-2: Profile (transverse section) of conical/pyramidal (left) and spherical (right) indenter tips.

A comparison is shown in Figure 2-3 for the projected contact area of the two indenter tips used in the current work, a Berkovich pyramidal tip and a 300 μm diameter spherical tip. For tests at very small displacement levels, tens of nm, the projected contact for the spherical tip is substantially greater than that of the Berkovich tip, while at displacements on the micron scale, the areas converge to a similar value for the two tips.

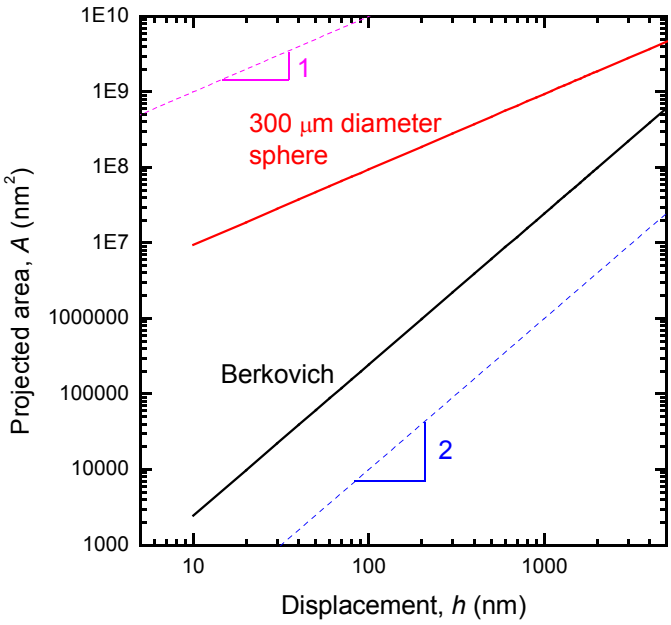

Figure 2- 3: Contact projected area (*A*) as a function of tip displacement into the sample (*h*) for a conical/pyramidal indenter tip and a 300 μm diameter spherical indenter tip.

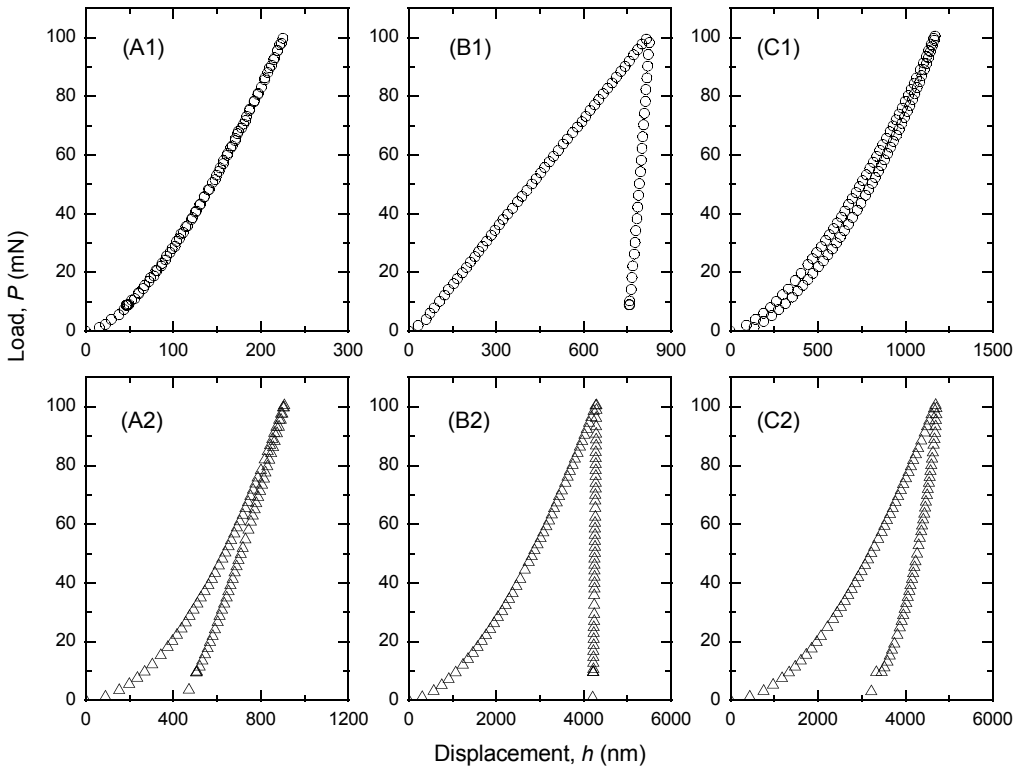

Figure 2-4: Indentation load-displacement (*P-h*) data for tests performed on the same three materials, under identical indentation loading rate conditions; (A) fused silica, (B) aluminum, and (C) PL-1 polymer. Tests were conducted with two different indentation tips, a 300 μm diameter sphere (top row, "1" labels) and a Berkovich pyramid (bottom row, "2" labels).

Indentation responses are shown in Figure 2-4for three materials (A) glass, fused silica; (B) metal, single-crystal aluminum; and (C) polymer, poly(methyl methacrylate) were tested with the same instrument under identical indentation conditions (100 mN peak load, 1 mN s^{-1} loading- and unloading- rate). Two different indenter tips were used, a 300 μm diameter spherical tip (top row, "1" labels) and a Berkovich pyramidal tip (bottom row, "2" labels). The displacement scale is larger for each material in the case of the Berkovich tip due both to the smaller contact areas at small depths and the immediate onset of plastic deformation. Details of the shapes of the indentation load-displacement responses for the different tip geometries will be discussed in the following sections.

2.1.2 Spherical Indenter (Hertzian) Solutions

Hertzian contact theory concerns the contact of two spherical bodies (called bodies 1 and 2) and for which the relationship between the load P applied to bring the two bodies into contact and the total deformation h of the two bodies is [Johnson, 1985]

$$h^{3/2} = \frac{3}{4\sqrt{R}} P \frac{1}{E_R} \qquad [2\text{-}1]$$

where R is the contact radius and E_R is the "reduced modulus". The values of R and E_R are both related to series combinations of the properties of the two individual bodies. The effective radius, R is defined as:

$$\frac{1}{R} = \frac{1}{R_1} + \frac{1}{R_2} \qquad [2\text{-}2]$$

and the reduced modulus, E_R is defined as:

$$\frac{1}{E_R} = \frac{1-\nu_1^2}{E_1} + \frac{1-\nu_2^2}{E_2} = \frac{1}{E'_1} + \frac{1}{E'_2} \qquad [2\text{-}3]$$

where ν_i is the Poisson's ratio and E_i is the elastic modulus for each body, and the combined term $E/(1-\nu^2)$ is the plane strain modulus (E') for each body. The contact dimension (radius) a is related to the effective radius (R) and total deformation (h) as:

$$a = (hR)^{1/2} \qquad [2\text{-}4]$$

In the case of indentation by a sphere onto a flat sample surface, the effective radius R is the indenter tip radius, since the sample radius is infinitely large relative to the small indenter tip. Indenter tips are also made of relatively stiff materials such that the

reduced modulus E_R is dominated by the sample modulus except for the case of very stiff samples.

For a perfectly elastic spherical indentation experiment, the load P is proportional to $h^{3/2}$ and a direct fit of Eqn. 2-1 to the fused silica load-displacement data gives a value of the reduced modulus (Fig. 2-5). Replotting the data from Fig. 2-5 on logarithmic coordinates demonstrates the power law (3/2) behavior (Figure 2-6).

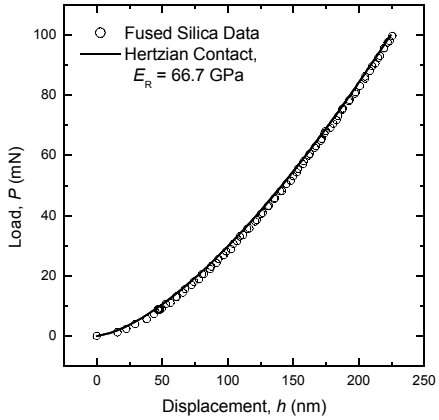

Figure 2-5: Perfectly elastic spherical indentation load-displacement (*P-h*) data for which the loading and unloading responses are indistinguishable. The solid line is a fit to Eqn. 2-1 for Hertzian contact on fused silica glass.

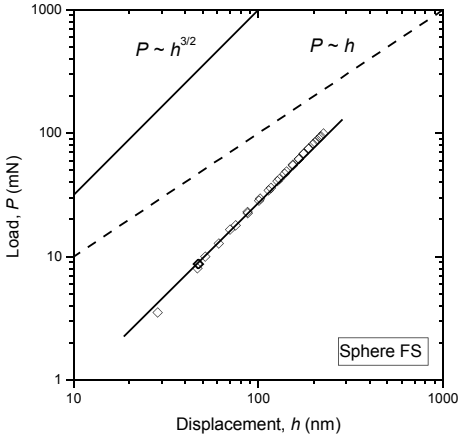

Figure 2-6: Spherical indentation load-displacement (*P-h*) data for purely elastic contact (here on fused silica) demonstrating the $P \sim h^{3/2}$ relationship from Eqn. 2-1.

For a spherical indenter tip, there is a point associated with the onset of yielding and a transition from elastic to plastic indentation behavior, evident by a change from $P \sim h^{3/2}$ behavior to $P \sim h$ behavior. This change is evident in aluminum; data from Figure 2-4 (subplot B1) have been re-plotted on a log scale along with lines indicating the two critical functional forms of the load-displacement relationship for spherical indentation. While the fused silica data retained the approximately $P \sim h^{3/2}$ behavior over the range of indentation depths (Figure 2-6), the aluminum data demonstrates the transition to $P \sim h$ behavior (Figure 2-7).

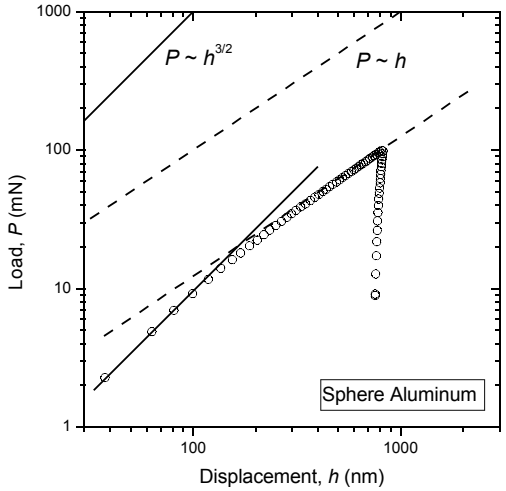

Figure 2-7: Spherical indentation load-displacement (*P-h*) data for elastic-plastic contact (here on aluminum) demonstrating the $P \sim h^{3/2}$ relationship from Eqn. 2-1 at small depths and $P \sim h$ behavior at larger depths.

2.1.3 Conical Indenter Solutions

The elastic load-displacement relationship for conical indentation is [Sneddon, 1965]:

$$h^2 = \frac{2\gamma^2}{\pi \tan\psi} P \frac{(1-\nu^2)}{E} \qquad [2\text{-}5]$$

where ψ is the included half-angle of the indenter tip and γ is a constant relating the total displacement h and the "contact displacement" h_c. (A similar distinction between h and h_c is present in the spherical indentation solution but this difference appears to be key in conical indentation, as will be discussed further in Chapter 3.) The contact displacement is slightly smaller than the total displacement h due to elastic deformation outside the contacted region (Figure 2-8).

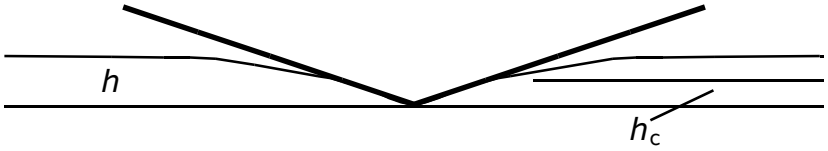

Figure 2-8: Berkovich pyramid indenting a deforming surface, leading to a tip contact depth h_c that is smaller than the total displacement h.

In conical/pyramidal indentation the plastic deformation shares the $P \sim h^2$ dependence of the elastic indentation relationship, such that the responses are uniformly quadratic, as shown in Figure 2-9 for Berkovich indentation tests on fused silica (FS) and aluminum. The onset of plastic deformation is typically occurs at very small depths and is not easily detectable in Berkovich indentation.

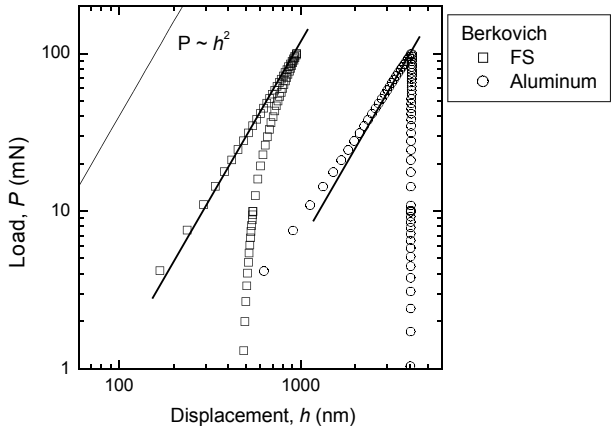

Figure 2-9: Berkovich pyramidal indentation load-displacement (*P-h*) data for elastic-plastic responses of fused silica and aluminum materials demonstrating approximately quadratic load-displacement behavior over the entire depth-range of the indentation test.

2.1.4 Oliver-Pharr Analysis

The last decade has seen rapid growth in the use of commercial contact mechanical testing devices ("nanoindenters"). A key feature of the commercialization of these instruments was the acceptance of a single technique ("Oliver-Pharr deconvolution", [Oliver and Pharr, 1992]) for obtaining elastic modulus from a conical/pyramidal indentation test data. This was an important development since the elastic and plastic deformation components in conical/pyramidal indentation share the same quadratic dependence of load on displacement, so it is impossible to separate these deformation components and obtain an elastic modulus directly from Eqn. 2-5. The elastic modulus is obtained in indentation testing by assuming that the unloading response is purely elastic, and relating the reduced modulus E_R to the unloading stiffness S via:

$$E_R = \frac{S\sqrt{\pi}}{2\sqrt{A_c}} \qquad [2\text{-}6]$$

In addition, by analogy with Vickers hardness testing and the pioneering work of Tabor [1951], the nanoindentation test results in a second property besides elastic modulus, the contact hardness, H_c (to be discussed at length in Appendix B):

$$H_c = \frac{P_{max}}{A_c} \qquad [2\text{-}7]$$

In both of these expressions appears the contact area (A_c), which is calculated from the contact displacement (h_c) via a calibration function of the form:

$$A_c(h_c) = C_0 h_c^2 + \sum C_k h_c^{1/2^{(k-1)}} \qquad [2\text{-}8]$$

In addition to the area function, there is an additional calibration-derived quantity, the

machine (frame) compliance C_f. The contact area function and the frame compliance are related, and the calibration protocol used to obtain these values will be discussed at length in Chapter 3.

Once the calibration (frame compliance and tip area function) is known, the analysis of elastic-plastic DSI data using the Oliver-Pharr protocol is straightforward. Three parameters are obtained directly from raw *P*-*h* data:

$$P_{\max}, h_{\max}, S = \frac{\mathrm{d}P}{\mathrm{d}h} \qquad [2\text{-}9]$$

as shown in Figure 2-10. The measured stiffness *S* is the combination of the sample stiffness and the frame stiffness or the sample compliance and frame compliance:

$$\frac{1}{S} = \frac{1}{S_{\text{sample}}} + \frac{1}{S_{\text{frame}}} \qquad [2\text{-}10]$$

$$S^{-1} = C = C_{\text{sample}} + C_{\text{frame}} \qquad [2\text{-}11]$$

where *C*, the compliance, is the inverse stiffness. The frame stiffness (or compliance) must be taken into account (subtracted off the measured stiffness or compliance) to accurately obtain sample elastic modulus from sample stiffness.

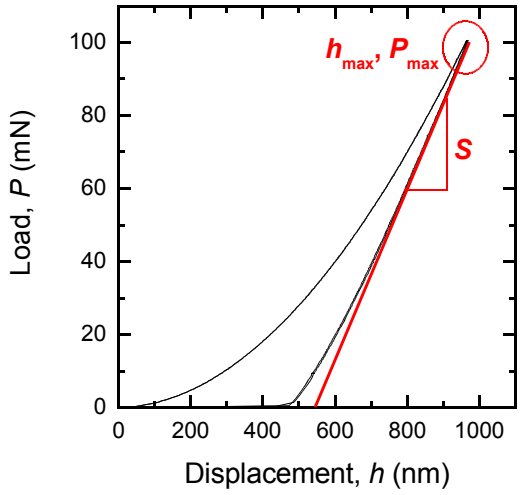

Figure 2-10: Fused silica elastic-plastic indentation traces showing parameters obtained directly from the raw load-displacement (*P*-*h*) data: the peak load (P_{max}) and displacement (h_{max}), and the unloading stiffness (*S*).

The total displacement (h) in an elastic-only system is the sum of the contact displacement h_c, the fraction of the displacement actually in contact with the indenter, and the surface displacements outside the indenter h_s (Figure 2-8):

$$h = h_s + h_c \qquad [2\text{-}12]$$

and the contact depth is defined by the elastic solution of Sneddon [1965]:

$$h_c = 2h/\pi \qquad [2\text{-}13]$$

for a pyramidal indenter. However, in elastic plastic indentation, the contact depth cannot be calculated directly via the total displacement, since the displacement contains both elastic and plastic contributions. Therefore the elastic contact depth must be inferred, and is usually done so by examination of the elastic stiffness *S*, in the analysis of Oliver and Pharr:

$$h_c = h_{max} - \epsilon \frac{P_{max}}{S} \qquad [2\text{-}14]$$

A value of $\epsilon = 0.75$ is typically used (this value is for a parabolic indenter but seems to 'work' better than the value of 0.72 for a conical indenter, [Oliver and Pharr, 1992]). The corresponding contact area $A_c(h_c)$ is calculated from the area calibration [Eqn 2-8] and used to calculate properties of reduced modulus E_R and contact hardness H_C:

$$E_R = \frac{S_{\text{sample}}\sqrt{\pi}}{2\sqrt{A_c}}$$
$$H_C = \frac{P_{max}}{A_c} \qquad [2\text{-}15]$$

In direct analogy to the Hertzian contact case (Eqn. 2-3), the reduced modulus E_R can be calculated as

$$\frac{1}{E_R} = \frac{1-\nu_I^2}{E_I} + \frac{1-\nu_S^2}{E_S} \qquad [2\text{-}16]$$

where I and S refer to the indenter tip and sample, respectively. The indenter tip is usually taken to have an elastic modulus of E > 1100 GPa and Poisson's ratio $\nu \sim 0.07$ if made of diamond. In the case of compliant materials, the indenter tip is effectively rigid compared to the sample $(E_I \gg E_S)$ such that the reduced modulus E_R is equal to the plane strain modulus of the sample, E^* or E':

$$E_R = E^* = \frac{E_S}{1-\nu_S^2} \qquad [2\text{-}17]$$

The cutoff for determining if this condition is true (e.g. if the indenter tip is enough

greater in modulus compared to the sample to be effectively rigid, such that Eqn. 2-17 holds) is around a sample modulus of 30 GPa for a diamond indenter tip, as shown in Figure 2-11.

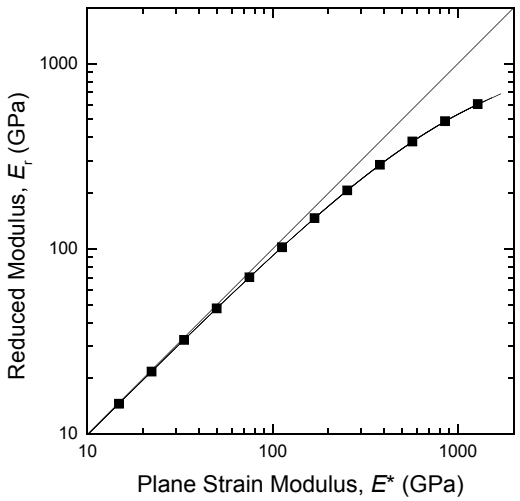

Figure 2- 11: Reduced modulus (E_R) as a function of sample plane-strain modulus (E^*), demonstrating that the indenter tip is effectively rigid for sample moduli of ~ 30 GPa or less.

2.1.5 Experiment Types for Indentation Testing

In contrast to traditional tensile mechanical testing, where the most simple and common test is monotonic loading to failure, any contact mechanical test will consist of a loading segment and an unloading segment to retract the indenter from the surface. Although the sample may undergo permanent deformation or cracking during a contact test, these tests are not associated with whole scale failure of the sample and are minimally- or non-destructive. In addition, a second key difference between contact mechanical testing and traditional tensile testing is that the loading input in tensile testing is usually displacement-control, with feedback-based load control, while in contact mechanical testing the loading input is load-control (and feedback-based displacement control has not become commonly adopted).

Different loading functions are used for different materials and for obtaining information about different aspects of material response. The focus here is on the three

most common contact test types used for materials exhibiting either time-independent or time-dependent behavior: (a) triangle-wave loading; (b) trapezoidal loading; (c) exponential loading (Figure 2-12). In triangle and trapezoidal loading, the loading and unloading rates (k) are constant and are usually the same for loading and unloading segments of the test, and the corresponding time period required to load and unload the sample (the "rise time", t_R or t_{RISE}) is fixed and related to the loading rate and peak load ($t_R = P_{max}/k$). The triangle-wave test is in fact the limiting case of trapezoidal loading with a zero second holding time at peak load (P_{max}). The exponential loading test is usually asymmetrically constructed, with exponential loading and constant-rate unloading. This test is most frequently associated with one instrument manufacturer (MTS) and will be discussed in additional detail in section 2.1.6.1 below.

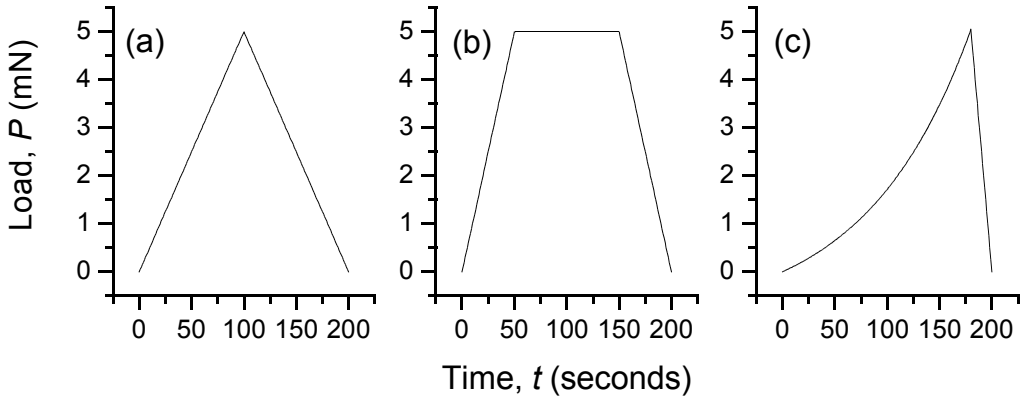

Figure 2- 12: Common load-time (*P-t*) testing inputs for nanoindentation contact mechanical tests (a) triangle-wave loading; (b) trapezoidal loading; (c) exponential loading.

2.1.6 Indentation Testing Instruments

There are several different companies producing commercial nanoindentation testing machines, of which two were utilized in the current work and will be briefly described in this section. The differences in physical design of the instruments made by MTS and Hysitron will be discussed briefly in the following sections, as they turned out

to be noteworthy in the experimental results presented later in this work.

2.1.6.1 MTS Nanoindenter XP

The MTS Nanoindenter XP has a speaker-coil drive for production of motive force, and independent capacitance gages for the measurement of indentation displacements. The fundamental components of the instrument are shown schematically in Figure 2-13. The maximum indentation force for this instrument is approximately 700 mN and the maximum indentation displacement is extremely large for a "nanoindenter", on the order of hundreds of micrometers. The minimum useful indentation force and displacement varies from instrument to instrument depending on the physical environment; in the current work the smallest working load used was 0.1 mN and the smallest indentation displacements considered quantitative were 30 nm.

In addition to the quasi-static indentation load, the MTS Nanoindenter has a feature, continuous stiffness measurement (CSM) in which a small sinusoidal oscillation at 45 Hz is superposed over the quasi-static load during the loading segment of any test type shown in Figure 2-12. The data from the oscillatory loading are analyzed separately from the quasi-static data to obtain modulus and hardness as a function of indentation depth. The exponential loading function (Figure 2-12c) is particularly useful in conjunction with this CSM feature in the measurement of thin-film samples for which the apparent elastic modulus varies as a function of indentation depth due to the influence of a modulus-mismatched substrate supporting the film. A limitation of this technique for polymeric materials is that the modulus measured in this manner is not a time-independent elastic modulus, but a frequency-dependent complex modulus.

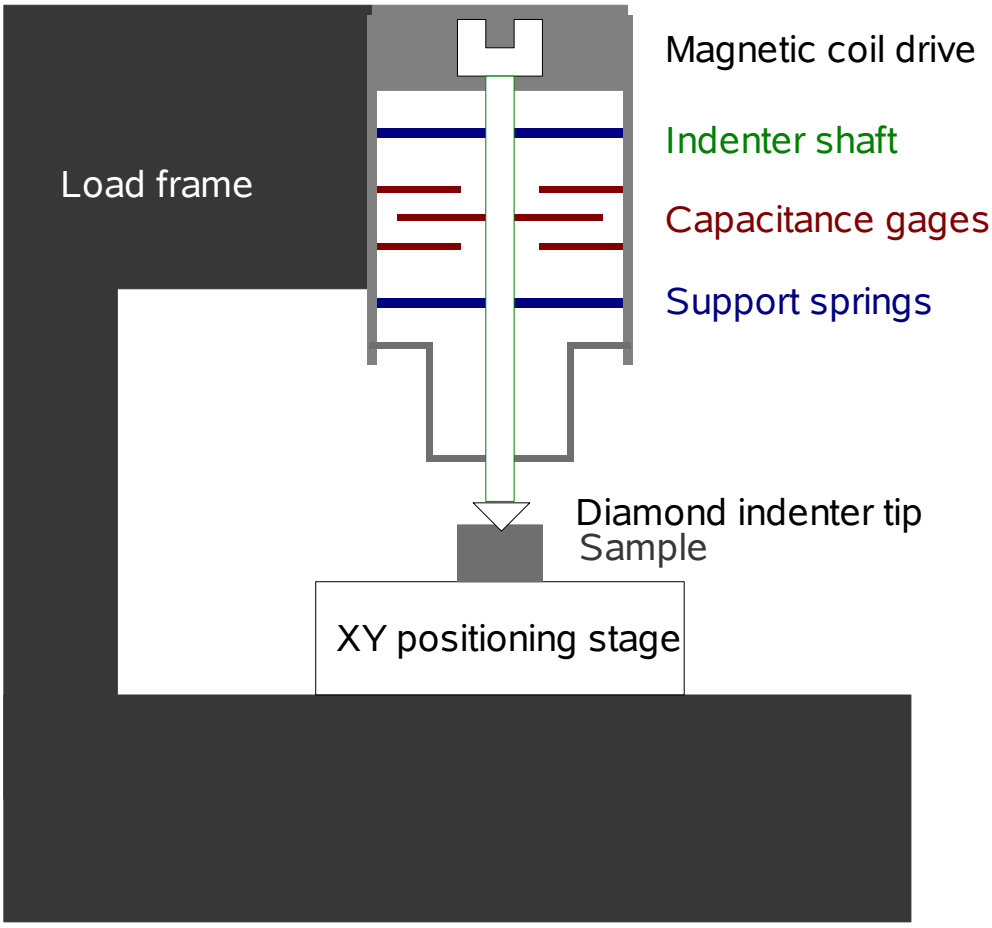

Figure 2-13: Schematic diagram of the MTS Nanoindenter XP [adapted from the MTS Nanoindenter XP Testworks 4 User Manual, (c) MTS Systems Corp.]

The exponential loading test (Figure 2-12c) is sometimes referred to as constant $\dot{P}/P$ as shown in Eqn. 2-18.

$$P(t) = P_0 \exp(rt)$$
$$P(t) = \frac{dP}{dt} = r P_0 \exp(rt) \qquad [2\text{-}18]$$
$$\frac{\dot{P}}{P} = r$$

This test type is used with continuous stiffness measurements (CSM) especially in the case of near-surface property differences, such as with thin films or with a polymer surface oxidation layer. The slow loading rate at small depths along with the acceleration at larger depths allows for good measurements of near-surface properties using this test type.

2.1.6.2 Hysitron Triboscope/Triboindenter

The Hysitron Triboscope and Triboindenter utilize the same indentation transducer, which incorporates a three-plate capacitive transducer for both motive force production and displacement measurement. The Triboscope is an independent transducer attached by the user to a scanning probe (atomic force) microscope while the Triboindenter is a stand-alone complete indentation testing machine made with similar components as the Triboscope-SPM/AFM system. The fundamental components of the Hysitron instruments are shown schematically in Figure 2-14, where the Triboindenter configuration is shown, and the alternative Triboscope configuration is presented as dashed lines. The maximum indentation force for this instrument using a standard transducer is approximately 12 mN and the maximum indentation displacement is only 2-3 micrometers. However, this instrument can also be used to scan the surface of the sample following the indentation test, using the piezoelectric transducer originally associated with the scanning probe microscopy configuration, and generate an image of the sample surface. This image is not as detailed as those obtained from traditional scanning probe microscopy, as the indentation tip is substantially larger and less sharp than AFM tips. Although the piezo scanner provides this advantageous sample imaging capability, it also adds to the complexity in the load train of the indentation instrument.

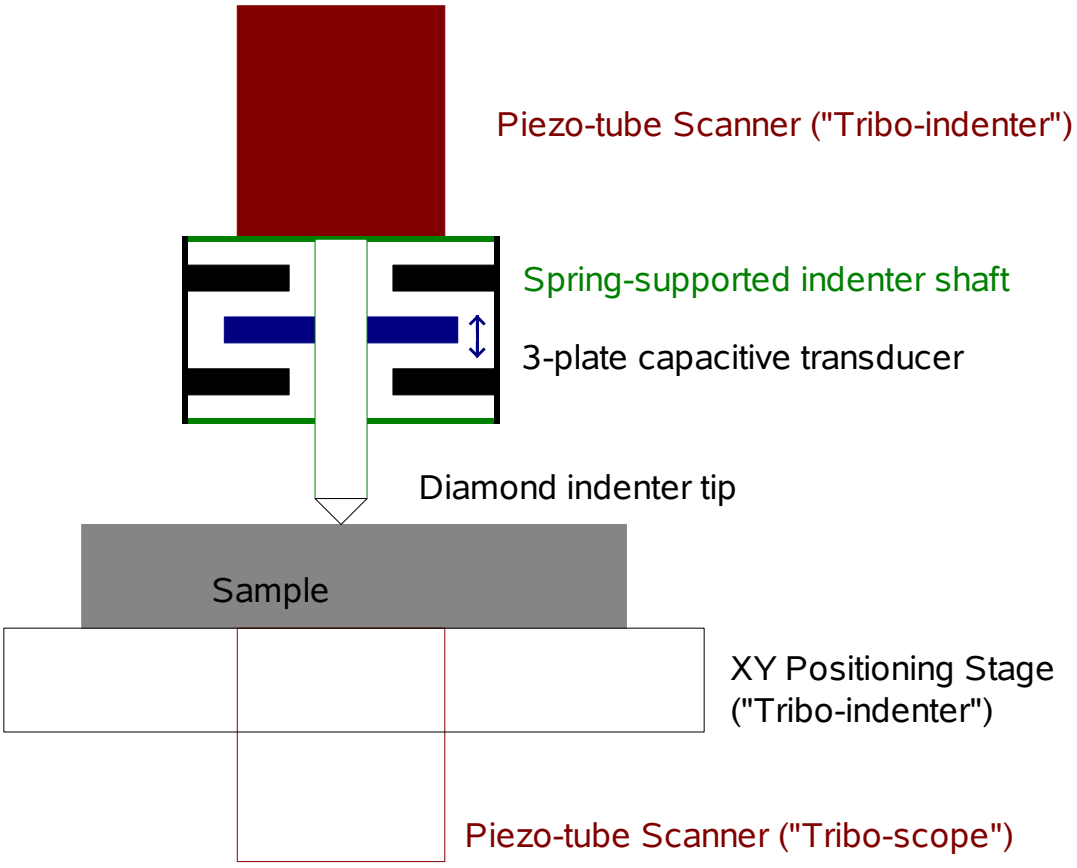

Figure 2-14: Schematic diagram of the Hysitron indentation system; drawing adapted from [Balooch et al, 1998]

2.2 Time-Dependent Mechanical Behavior

Time-dependent mechanical behavior is inherently inelastic: the stress-strain relationship for a material is an explicit function of time under finite loading conditions. This time-dependence results in deformation at fixed load or stress (creep), relaxation of load or stress at fixed deformation or strain, and apparent rate-dependence in mechanical properties. There is also an energy dissipation under cyclic load. There are model-independent measures of time-dependent behavior, as well as models for explicitly characterizing the time dependence in terms of material time constant (τ) or viscosity (η) parameters.

2.2.1 Model-Independent Measures of Time-Dependence

A characteristic feature of most time-dependent mechanical analyses is the requirement that a type of model be selected *a priori*. There are, however, ways to characterize time-dependence without making an *a priori* model selection, and two types of model-independent characterizations will be briefly described here.

The first simple comparison between time-dependent responses is in the direct quantification of the extent of creep or relaxation. As shown in Figure 2-15, the load (F, or stress σ) at some time t can be compared to the load at the beginning of relaxation, F_0, taken at $t = 0$. This is most typically done by calculating a relaxation fraction, or $F(t)/F_0$. Similarly, for the case of creep, the extent of the creep can be quantified by examining the creep displacement (δ, or creep strain ε) compared to the displacement at $t = 0$. In this case, the most commonly examined parameter is the total creep displacement, $\delta(t) - \delta_0$. These simple measurements are best employed for first principles comparisons of materials tested under the same loading or displacing conditions.

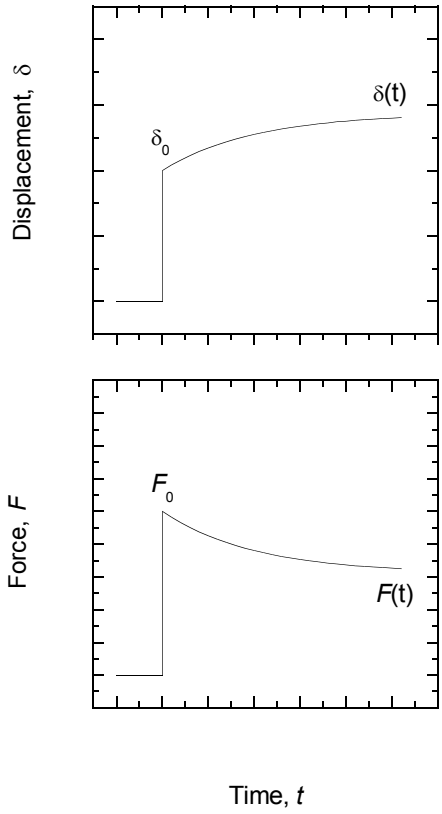

Figure 2-15: Schematic diagram of parameters compared to determine extent of time-dependent mechanical response. The load $F(t)$ or displacement $\delta(t)$ at some time t is compared with the initial load or displacement at t = 0 (F_0 or δ_0).

Another model-independent measurement of the time-dependent response, particularly useful in a cyclic test is hysteresis energy. As demonstrated in Figure 2-16, the hysteresis loop work (L) is the shaded region, while the total mechanical work input at peak load (T) is the hatched region. One mechanism to compare these parameters is a dissipation ratio, D, in which the hysteresis energy is divided by the total loading energy to give the fraction of energy dissipated in the cycle. For slower loading in a time-dependent material, typically more energy is dissipated in the cycle and the dissipation ratio increases.

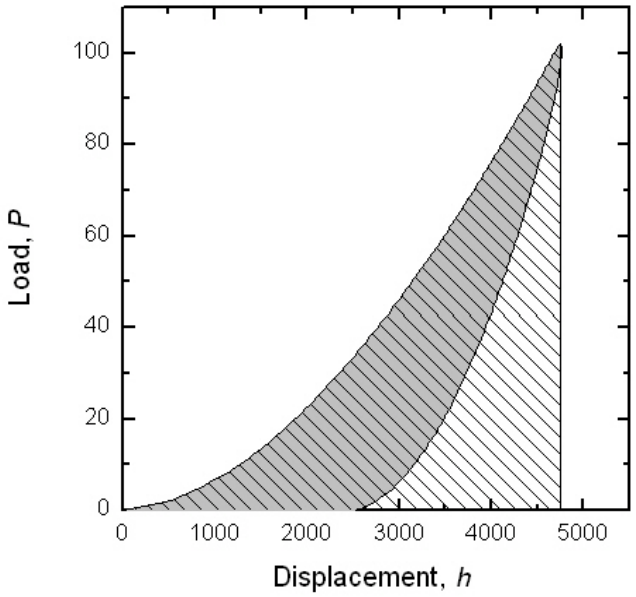

Figure 2-16: Schematic diagram of hysteresis energy calculation for a load-unload cycle. The grey region is the hysteresis loop work (*L*), while the hatched area is the total work on loading (*T*). The fractional energy dissipation (*D*) is the ratio of the loop work to total work (*L*/*T*).

2.2.2 Viscoelastic Spring-Dashpot Models

Next, simple viscoelastic models [Findley et al, 1989] are examined. Two fundamental mechanical elements are used to describe viscoelastic mechanical behavior: a linear (Hookean) spring (Figure 2-17, top) and a linear (Newtonian) dashpot (Figure 2-17, bottom). The Young's modulus E for a linear elastic material may be considered as a spring constant and the viscosity η may be considered as a dashpot coefficient.

Since the constitutive equation for a spring, $\sigma = E\varepsilon$, has no time dependence, no linear combination of springs in series or parallel can be used to give time dependence to a material . Combinations of one spring and one dashpot element either in series (Maxwell element, Figure 2-18 i) or in parallel (Kelvin elements, Figure 2-18 ii) give rise to the simplest viscoelastic constitutive equations, which can be used to describe the time-dependent mechanical behavior of materials such as polymers and biological

materials. These two-element combinations result in constitutive models that are first-order ordinary differential equations in time. More complicated but also more physically realistic models for time-dependent behavior are shown in Figure 2-18 iii, the 3-parameter Standard Linear Solid (SLS), and Figure 2-18 iv, the 4-parameter Burgers material (whose constitutive model is a second order differential equation due to the two dashpot elements; the other models in Fig. 2-18 give rise to first order differential equations).

$$\sigma = E\,\epsilon$$

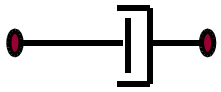

$$\sigma = \eta \frac{\mathrm{d}\,\epsilon}{\mathrm{d}\,t}$$

Figure 2- 17: Linear Hookean spring (top) and Newtonian Dashpot (bottom) mechanical elements shown as schematic illustrations along with each element's constitutive law in terms of stress (σ) and strain (ε).

For most analyses, the differential form of the constitutive equation is solved once, in either creep or stress-relaxation following a step perturbation, in order to arrive at a creep or relaxation function for the material model. For frequently used models, such as those shown in Figure 2-18, these solutions are well-known [Findley et al, 1989]. The creep or relaxation function can then be used in conjunction with Boltzmann superposition integral operators to solve for full stress-strain-time responses under arbitrary loading conditions, as will be discussed in section 2.2.3.

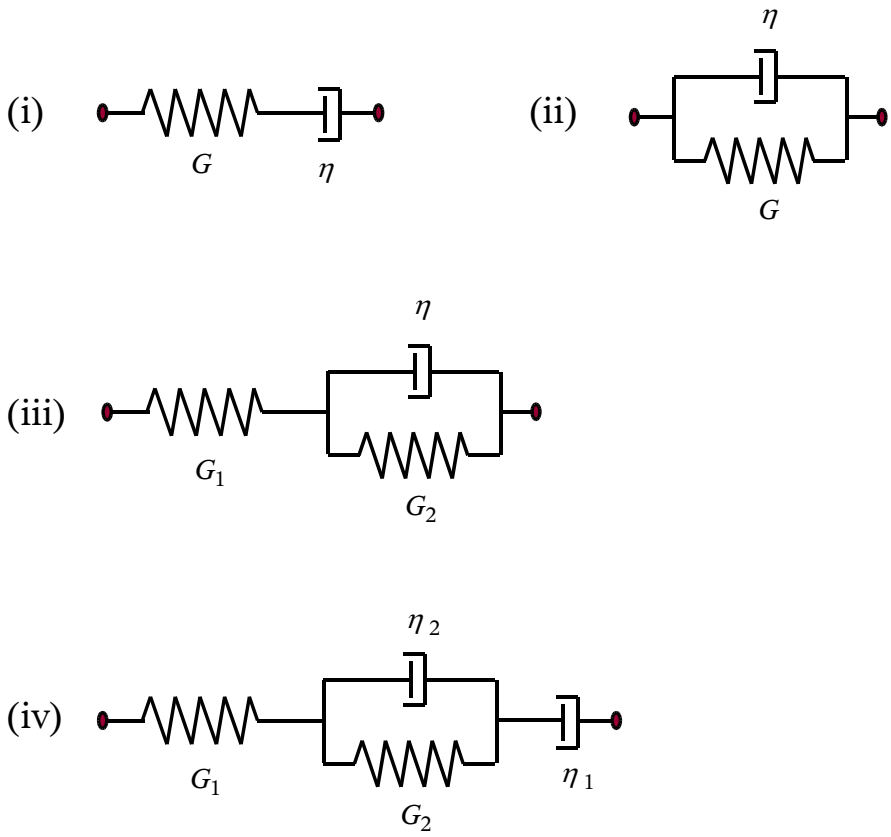

Figure 2-18: Simple combinations of spring (G_i) and dashpot (η_i) elements give common viscoelastic models (i) Maxwell fluid; (ii) Kelvin solid, (iii) Standard Linear Solid, (iv) Burgers material

Viscoelasticity is frequently associated with stresses and strains occurring in the deviatoric (shear) components of the stress and strain tensors [Cheng et al, 2000]. As such, the elastic components in viscoelasticity can be re-written in terms of shear moduli G_i. The shear modulus G can be related to the uniaxial elastic modulus E by:

$$G = \frac{E}{2(1+\nu)} \qquad [2\text{-}19]$$

where ν is the Poisson's ratio. The simplest applied loading condition for a time-dependent material is the sudden application of a constant stress or strain perturbation.

The relaxation function $G(t)$ for a material describes how the force or stress on the material decreases with time under a constant displacement or strain perturbation. The relaxation function is a time-dependent version of the elastic modulus, predicting the stress response $\sigma(t)$ for a step change in strain ε_o:

$$\sigma(t) = G(t)\varepsilon_o \qquad [2\text{-}20]$$

The creep function $J(t)$ is the analogous function for describing the lengthening (creep) $\varepsilon(t)$ of a material at constant stress σ_o:

$$\varepsilon(t) = J(t)\sigma_o \qquad [2\text{-}21]$$

The creep function is similar to a compliance coefficient for time-independent systems. As in linear elastic materials, where the stiffness S and compliance C are directly related

$$S = 1/C \qquad [2\text{-}22]$$

The creep and relaxation functions are also related for a linear viscoelastic material [Lakes and Vanderby, 1999]:

$$sG(s) = 1/\,sJ(s) \quad \text{or} \quad G(s)J(s) = s^{-2} \qquad [2\text{-}23]$$

where s is the time-transformed variable of Laplace space [Findley et al, 1989].
It has been established that the relaxation response $G(t)$ of many materials, and particularly biological materials, can be fit by a series of exponential decays [Macosko, 1994; Fung, 1993], each associated with two parameters, a time constant τ_i and a weighting coefficient G_i that is associated with a shear stiffness:

$$G(t)=\sum_i G_i \exp\left(\frac{-t}{\tau_i}\right) \qquad [2\text{-}24]$$

This equation is a generalized relaxation for a fluid, since it allows for eventual relaxation to a zero stress state; a solid will relax to an intermediate equilibrium stress state and therefore the relaxation function must include an additional constant term G_e representing the equilibrium elastic response.

$$G(t)=G_e+\sum_k G_k \exp\left(\frac{-t}{\tau_k}\right) \qquad [2\text{-}25]$$

For the most commonly used mechanical model, an SLS (Figure 2-18iii), $k = 1$ in Eqn. 2-25 and the parameters can be described in terms of the spring constants G_1 and G_2 such that the relaxation function $G(t)$ is

$$G(t)=\frac{G_1}{G_1+G_2}\left\{G_2+G_1 \exp\left(\frac{-t}{\tau_R}\right)\right\} \qquad [2\text{-}26]$$

where the time constant under relaxation conditions, τ_R, is

$$\tau_R=\eta/(G_1+G_2) \qquad [2\text{-}27]$$

For creep of a standard linear solid, the creep function is

$$J(t)=\frac{1}{G_1}+\frac{1}{G_2}\left(1-\exp(-t/\tau_C)\right) \qquad [2\text{-}28]$$

where the time constant under creep conditions τ_C is

$$\tau_C = \eta / G_2 \qquad [2\text{-}29]$$

and the corresponding generalized creep function for multiple time constants is

$$J(t) = C_0 - \sum_{i=1}^{j} C_i \exp(-t/\tau_i) \qquad [2\text{-}30]$$

where the C parameters are associated with compliance values (inverse shear moduli).

2.2.3 Linearly Viscoelastic Behavior

Once the creep or relaxation function for a material has been identified, it can be used to describe and/or predict the behavior of that material under different types of loading. According to Boltzmann Superposition [Findley et al, 1989], the stress in a viscoelastic material (under uniaxial loading) at any time *t* can be determined by integrating over the relaxation function and strain history dϵ/d*t*:

$$\sigma(t) = \int_0^t G(t-u) \frac{\mathrm{d}\epsilon}{\mathrm{d}u} \mathrm{d}u \qquad [2\text{-}31]$$

where *u* is a dummy variable for time. Conversely, the strain can be found by integrating over the creep function and the stress history:

$$\epsilon(t) = \int_0^t J(t-u) \frac{\mathrm{d}\sigma}{\mathrm{d}u} \mathrm{d}u \qquad [2\text{-}32]$$

In extensive variables, Eqns. 2-31 and 2-32 can be written in terms of loads and displacements instead of stresses and strains:

$$P(t)=\int_0^t g(t-u)\frac{\mathrm{d}\,\delta}{\mathrm{d}\,u}\mathrm{d}\,u \qquad [2\text{-}33]$$

$$\delta(t)=\int_0^t j(t-u)\frac{\mathrm{d}\,P}{\mathrm{d}\,u}\mathrm{d}\,u \qquad [2\text{-}34]$$

where $g(t)$ and $j(t)$ are the relaxation or creep functions in extensive coordinates. The hereditary integrals are and extremely flexible way to solve for complicated input conditions, such as cyclic loading or sequential creep- or relaxation- tests at multiple levels.

2.3 Mechanical Properties of Composite Materials

Composite materials, both naturally-occurring and engineering composites, are inhomogeneous materials with independent phases of dissimilar materials. Composites have properties that are a compromise between the component materials, a quality exploited in the generation of new materials with properties unavailable in any other material. Many composites, both natural and artificial, consist of a ductile, compliant matrix (metal or polymer) with stiff, brittle particles. Bone may be similar to polymer matrix composites (PMCs) with glass bead reinforcements, bone is sometimes considered as having a compliant collagen network reinforced with hydroxyapatite particles [Jager and Fratzl, 2000; Kotha and Guzelsu, 2002] as will be discussed later in this work. The hydroxyapatite particles are stiff and brittle, while the collagen network is extremely compliant, ductile and tough. An interesting difference between bone and PMCs is that in PMCs the elastic modulus mismatch is about an order of magnitude between the two component materials ($E_{\text{polymer}} \sim 5$ GPa, $E_{\text{glass}} \sim 75$ GPa) whereas in bone the mismatch is perhaps greater, 2-3 orders of magnitude ($E_{\text{mineral}} \sim 150$ GPa, $E_{\text{Collagen}} \leq 1.5$ GPa). The detailed examination of mineralized tissues as composite materials will be discussed at length in Chapter 5; fundamental scaling laws for composite mechanics are presented here for any two-phase composite.

2.3.1 Physical Properties of Composite Materials

Properties of a composite material are weighted combinations of the component properties [Chawla, 1987]. The characteristic properties for quantifying each phase (i) are the volume (v_i) and weight (w_i). The combination of these properties, the density $(\rho_i = w_i / v_i)$, is also frequently used to characterize the phases. From these fundamental properties one can calculate the weight fraction (W_F) or volume fraction (V_F) for the particle or filler phase (f or F):

$$W_F = \frac{w_F}{w_M + w_F} \quad [2\text{-}35]$$

$$V_F = \frac{v_F}{v_M + v_F} \quad [2\text{-}36]$$

where the subscript M is used to indicate the matrix or reinforced phase.

A rule-of-mixtures approach is a first approximation to describe the composite in terms of the component phases. For example, the density of the composite (ρ_c) is related to the density and volume fraction of the component phases by:

$$\rho_c = \rho_F V_F + \rho_M V_M \quad [2\text{-}37]$$

There is a simple relationship between weight fraction and volume fraction for two phase composite (assuming no porosity):

$$V_F = \frac{w_F}{w_M\left(\frac{\rho_f}{\rho_M}\right) + w_F} = \frac{1}{\left[1 + \frac{\rho_F}{\rho_M}\left(\frac{1}{W_F} - 1\right)\right]} \quad [2\text{-}38]$$

For a two phase material *with* porosity, there is no change in the weight fraction expression but there is a volume contribution from the weightless pores (where v_P is the pore volume):

$$V_F = \frac{v_F}{v_M + v_F + v_P} \quad [2\text{-}39]$$

2.3.2 Elastic Modulus of Composite Materials

Many material properties of a composite material, including the elastic modulus, are typically expressed as the volume-fraction weighted combination of the component phase properties. In the simplest approximation for elastic modulus, the two components are volume fraction-weighted series or parallel springs. The two combinations (series and parallel) form extreme bounds on the actual composite's behavior, and these simple bounds for two-phase composites are frequently called Voigt-Reuss bounds. The upper (iso-strain, parallel springs, Voigt) and lower (iso-stress, series springs, Reuss) bounds are [Chawla, 1987]:

$$E_{\mathrm{U}} = V_2 E_2 + (1 - V_2) E_1 \qquad [2\text{-}40]$$

$$E_{\mathrm{L}} = \left(\frac{V_2}{E_2} + \frac{(1 - V_2)}{E_1} \right)^{-1} \qquad [2\text{-}41]$$

where by convention $E_2 > E_1$ and $V_1 + V_2 = 1$. These bounds are frequently used to describe the longitudinal (upper bound) and transverse (lower bound) moduli of oriented fiber-reinforced composites with fibers aligned in one primary direction.

A second common set of bounds for composite materials are the Hashin-Shtrikman bounds, which have been found to be more physically realistic for many composites, particularly those in which the reinforcing phase is particulate and not continuous aligned fibers. These bounds are formulated in terms of the shear and bulk moduli *G* and *K,* remembering that

$$G = \frac{E}{2(1+\nu)} \quad \text{and} \quad K = \frac{E}{3(1-2\nu)} \qquad [2\text{-}42].$$

The lower bounds are [Kingery et al, 1976]:

$$K_L = K_1 + V_2\left(\frac{1}{(K_2 - K_1)} + \frac{3(1-V_2)}{3K_1 + 4G_1}\right)^{-1}$$

$$G_L = G_1 + V_2\left(\frac{1}{(G_2 - G_1)} + \frac{6(K_1 + 2G_1)(1-V_2)}{5G_1(3K_1 + 4G_1)}\right)^{-1} \qquad [2\text{-}43]$$

$$E_L = \frac{9K_L G_L}{3K_L + G_L}$$

and the upper bounds are [Kingery et al, 1976]

$$K_U = K_2 + (1-V_2)\left(\frac{1}{(K_1 - K_2)} + \frac{3V_2}{3K_2 + 4G_2}\right)^{-1}$$

$$G_U = G_2 + (1-V_2)\left(\frac{1}{(G_1 - G_2)} + \frac{6(K_2 + 2G_2)V_2}{5G_2(3K_2 + 4G_2)}\right)^{-1} \qquad [2\text{-}44]$$

$$E_U = \frac{9K_U G_U}{3K_U + G_U} \cdot$$

A comparison of the Voigt-Reuss (V-R) and Hashin-Shtrikman (H-S) bounds is shown in Figure 2-19 for a stiff phase with E_2 = 100 GPa and a modulus mismatch factor (E_2/E_1) of 10, 100, and 1000. The difference between the upper and lower bounds (either V-R or H-S) increases with increasing modulus mismatch, making it increasingly difficult to predict the expected behavior of the composite material without *a priori* knowledge of the mechanism of strain transfer between the two different phases. The two variations (V-R or H-S) on the lower bound expression become indistinguishable (on linear coordinates) at large modulus mismatch, but the upper bounds remain distinct.

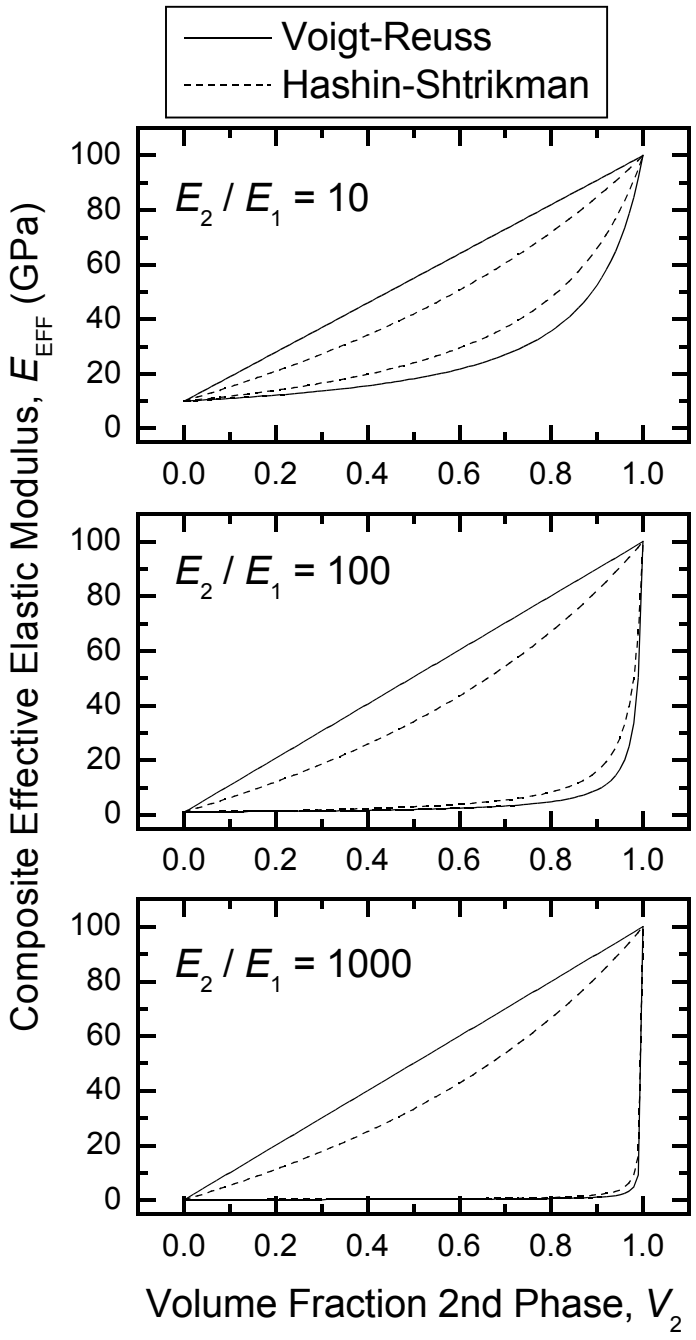

Figure 2-19: Elastic Modulus bounds for a material with E_2 = 100 GPa and E_1 = 10, 1, or 0.1 GPa for modulus mismatch (E_2 /E_1) factors of 10, 100, or 1000.

2.4 Finite Element Analysis

2.4.1 Introduction and Discretization

There are explicit analytical solutions within the theory of elasticity [Timoshenko and Goodier, 1934] for relatively few complete problems. The methodology required to solve these problems analytically is in many ways an art. Most modern mechanical analyses rely heavily on computational techniques, the most popular being finite element analysis (FEA). In FEA, a domain of material being simulated under some applied loading condition is discretized (divided) into individual segments called elements (lines in 1D, squares or triangles in 2D, tetrahedra or cubes in 3D; Figure 2-20). The elasticity equations (or any set of differential equations) are solved numerically in each elemental domain, and the complete solution to the original problem is found via the combination of these individual solutions, incorporating continuity across the element boundaries and agreement with boundary conditions applied to the entire body in the original problem statement. (For extensive discussion of the mathematical details and computer implementation of this process, the reader is referred to a basic text, such as "An Introduction to the Finite Element Method" by J.N. Reddy [1993].) FEA is particularly useful in problems with complicated geometry and in problems where the material properties vary from point to point within the domain.

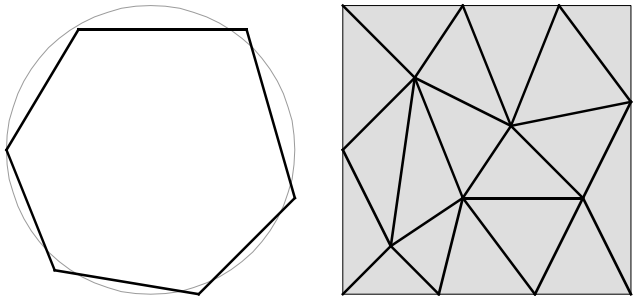

Figure 2-20: Domain discretization in one dimension (left) and two dimensions (right)

Thanks to advances in computer technology, FEA problems that once required the

use of a supercomputer can now be solved on a desktop or laptop consumer PC. There are a number of commercially available codes for which the mathematical details of solving the element equations are completely hidden from the user. In these commercial codes, the user specifies the type of problem, the geometry of the domain, the material properties in each region of the domain, the applied loading and boundary conditions, and in some cases information about the desired output parameters from the model, and the problem is then solved by the commercial code. The user may or may not have considerable control over the details of the discretization (the FEA "mesh"). Different programs utilize different input and output options for transmitting this information, some based dominantly on a graphical user interface (GUI) and others using plain text programming language. In the current work, the program FlexPDE [PDE solutions, Antioch, CA] was utilized for all FEA modeling and analysis. FlexPDE utilizes a text-based custom programming language and allows for substantial control over the geometry, material properties, and form of the output, but does not allow for much direct user-control of the discretized mesh. Thus, the program is both a mesh generator and numerical solver.

As mentioned above, the FEA calculations are, in the case of elasticity problems, based on solving the partial differential equations (PDEs) that provide the basis of elasticity theory and describe the relationships between stress, strain, and deformation (displacement) components in three dimensions. These basic relationships will be discussed briefly in the following sections for fully three-dimensional and two-dimensional plane-strain problems. For a more thorough discussion of the elasticity backbone of the finite element method, the reader is referred to Timoshenko and Goodier [1934] or any other fundamental elasticity text.

2.4.2 Fully 3D Problems

The relationships between stress, strain, and displacement presented in Chapter 1 within the context of a tensile test are an extremely simplified and one dimensional view

of elastic mechanics. A fully three-dimensional elasticity problem involves fifteen variables: six stress components (σ_{ij}), six strain components (ϵ_{ij}) and three displacement components (u_i) where $i, j = 1,2,3$ for the x-, y-, and z- directions.

For isotropic elasticity, the relationship between stress and strain components is more complicated than $\sigma = E\varepsilon$:

$$\tau_{ij} = \lambda \epsilon_{kk} \delta_{ij} + 2\mu \epsilon_{ij} \qquad [2\text{-}45]$$

where λ and μ the Lamé constants—two constants which can be related to the elastic modulus (E) and Poisson's ratio (ν) and that are frequently more convenient to use in analytical elasticity problems. The Lamé constants (λ,μ) can be easily related to the more experimentally common constants (E,ν) by:

$$\lambda = \frac{\nu E}{(1+\nu)(1-2\nu)} \qquad [2\text{-}46]$$

$$\mu = \frac{E}{2(1+\nu)}$$

Note that the second Lame constant(μ) is equivalent to the shear modulus (G).

The relationship between strain components and displacements is

$$\epsilon_{ij} = \frac{1}{2}(u_{i,j} + u_{j,i}) \qquad [2\text{-}47]$$

where repeated indices are used to denote the Einstein summation convention, and commas are used to indicate differentiation.

The equation for equilibrium in three-dimensions is

$$\tau_{ij,i}+F_i=0 \qquad [2\text{-}48]$$

where F_i are body forces.

2.4.3 Plane Strain Problems

In problems of plane strain, a two-dimensional formulation is used in which it is assumed that the thickness of the section is large in the third dimension and therefore displacement components in the third (x_3) dimension are zero.

$$\begin{aligned} u_1&=u_1(x_1,x_2)\\ u_2&=u_2(x_1,x_2)\\ u_3&=0 \end{aligned} \qquad [2\text{-}49]$$

This simplification reduces the number of relevant strain components from six to three:

$$\begin{aligned} \epsilon_{11}&=u_{1,1}\\ \epsilon_{22}&=u_{2,2}\\ \epsilon_{12}&=\frac{1}{2}(u_{1,2}+u_{2,1})\\ \epsilon_{13}&=\epsilon_{23}=\epsilon_{33}=0 \end{aligned} \qquad [2\text{-}50]$$

and stresses for isotropic elasticity from six to four.

$$\begin{aligned} \tau_{11}&=(\lambda+2\mu)u_{1,1}+\lambda u_{2,2}\\ \tau_{22}&=(\lambda+2\mu)u_{2,2}+\lambda u_{1,1}\\ \tau_{12}&=\mu(u_{1,2}+u_{2,1})\\ \tau_{13}&=\tau_{23}=0\\ \tau_{33}&=\lambda(u_{1,1}+u_{2,2})=\nu(\tau_{11}+\tau_{22}) \end{aligned} \qquad [2\text{-}51]$$

There are then two differential equations for the stress-displacement form of equilibrium:

$$\begin{aligned}\tau_{11,1}+\tau_{12,2}+F_1&=0\\ \tau_{12,1}+\tau_{22,2}+F_2&=0\end{aligned} \qquad [2\text{-}52]$$

and these two second order differential equations in two unknowns, u_1 and u_2, are what is solved numerically in plane strain finite element problems.

2.5 Mechanical Directions for this Work

Key background topics in experimental and analytical mechanics have been introduced in this chapter: (1) indentation contact mechanics, (2) analytical viscoelasticity, (3) mechanics of composite materials, and (4) finite element analysis. These topics have been introduced with primarily text-book (and classic paper) fundamentals; these are established fields of inquiry. In the remainder of this work, forming the bulk of the new investigation, these topics will be combined. Chapter 3 addresses experimental results for indentation of composite materials. In Chapter 4, a framework is developed for indentation of viscoelastic materials. Chapters 5 and 6 utilize finite element modeling to examine mechanics of composite materials, including an analysis of indentation of composite materials.